Design of Electromagnetic Bandgap Cavities for High-Gradient On-Axis Coupled-Cavity Linear Accelerators

Dario Laneve[ID], Vincenza Portosi[ID], Mario Christian Falconi, *Student Member, IEEE*, Giovanni Rutigliani, Raffaele Andrea Prisco, Vincenzo Dimiccoli, and Francesco Prudenzano[ID]

Abstract—The design of suitable electromagnetic bandgap (EBG) cavities has been performed by means of a hybrid numerical/analytical approach implemented via a homemade code with the aim of optimizing a novel accelerating structure for proton linear accelerators (linacs). In particular, a 3-GHz proton linac tank with on-axis coupled EBG cavities closed with full-end cells has been optimized. The proton beam input energy is 27 MeV. The performances of the proton linac EBG accelerating cavities have been compared with the performances of 27-MeV 3-GHz side-coupled proton linac accelerating cavities in terms of typical linac figures of merit. The use of EBG cavities allows to increase the transit time factor (by about 8%). Moreover, the peak surface electric field is strongly reduced (by about 65%), paving the way to the design of very high accelerating gradient microwave proton linacs. Furthermore, the wakefields of the EBG structure have been compared with those of the SCL structure, showing that the EBG structure provides effective damping of the transverse wakefields.

Index Terms—Accelerator cavities, electromagnetic bandgap (EBG) cavities, electromagnetic modeling, evolutionary optimization, linear accelerators (linacs), microwave devices, resonators.

I. INTRODUCTION

ELECTROMAGNETIC bandgap (EBG), or photonic bandgap (PBG), structures consist of periodic arrays (lattices) of metallic and/or dielectric elements, which prevent the electromagnetic propagation in a particular frequency band referred to as bandgap. The EBG structures can be engineered to design devices with unique properties, not achievable by using conventional geometries. EBG structures are typically used as frequency-selective resonating devices in

a wide range of both low- and high-power microwave applications, including electromagnetic noise suppression [1], [2]; millimeter-range waveguides [3]; bandpass filters [4]–[6]; antennas [7]–[9]; liquid sensor [10]; and particle linear accelerators (linacs) [11]–[18].

In linac applications, EBG resonators were used to design and fabricate metallic [11]–[14] and dielectric–metallic (hybrid) [15]–[18] traveling-wave disk-loaded linacs. EBG linac cavities support single-mode resonance, allowing the confinement of the fundamental TM_{010}-like accelerating mode in the lattice defect, while the higher order modes (HOMs) are unconfined. This is a significant advantage since the HOM wakefields can be suppressed, enhancing the accelerated beam stability [19], [20]. Moreover, a high accelerating gradient can be achieved in EBG-based linacs. As examples, an accelerating gradient of 35 MV/m was measured in a 17-GHz six-cell EBG electron linac [12] and an accelerating gradient of 89 MV/m with low breakdown probability was measured in a similar EBG accelerator structure [14]. However, we underline that no feasibility investigations have yet been done concerning the design of EBG-based standing-wave coupled-cavity linacs for accelerating heavy ion beams, such as proton beams.

In this article, for the first time, to the best of our knowledge, a novel on-axis coupled EBG proton linac is designed. In particular, the design of a 27-MeV 3-GHz standing-wave EBG linac tank closed with full-end cells is performed, where 27 MeV is the proton beam input energy. A hybrid numerical/analytical approach (HA), implemented via homemade computer code, is exploited for the design of the EBG tank. The HA computer code integrates a full 3-D finite-element method (FEM) investigation with an analytical model that accurately takes into account the periodic structure of the linac tank. A multi-objective particle swarm optimization (PSO) technique is also used to find the optimal geometry of the linac cavities with respect to the design specifications. The developed HA code is general and it can be employed for the design of a wide range of resonant structures, allowing a very efficient and automated design. The HA code has already been successfully used and experimentally validated for designing the conventional cavities of a 27-MeV 3-GHz side-coupled linac (SCL) [21]. The typical linac figures of merit pertaining to the EBG accelerating cavities have been compared with those pertaining to the SCL accelerating cavities. The EBG cavities allow increasing the transit-time factor (by about 8%)
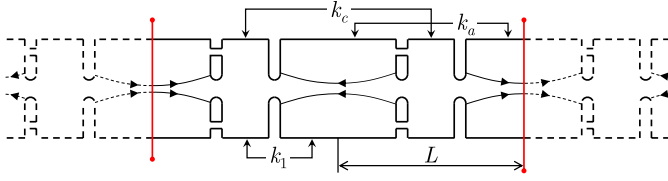
Fig. 1. Sketch of a general five-cavity (quintuplet) on-axis CCL closed with half ACs. The red lines are the conducting metal planes used to build the half ACs. The dashed-line cavities result from the mirror effect of the metal planes. The unexcited (coupling) cavities and septums (walls) act as drift tubes. The accelerating period is L.
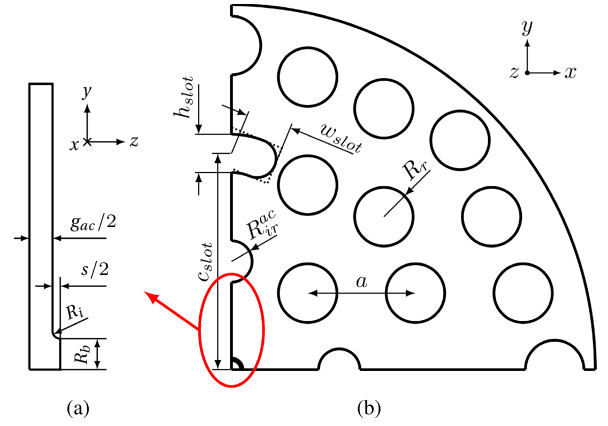

Fig. 2. Sketches of the (a) transversal and (b) longitudinal cross sections of an EBG accelerating cavity. One-eighth of the total inner (vacuum) volume is shown. The rods overlapping with the coupling slot area are removed from the cavity. The geometrical parameters are listed in Tables I and III.

in addition to a significant reduction (by about 65%) of the maximum surface electric field, paving the way to the design of high accelerating gradient proton linacs with low RF breakdown probability. The larger transversal dimensions of the EBG cavities and the on-axis coupling configuration suggest considering higher working frequencies in order to compensate for the 30% lower effective shunt impedance. Furthermore, the longitudinal and transverse wake potentials and impedances of EBG and SCL cavities have been simulated and compared. The simulation results show that the EBG cavities provide effective wakefield damping relative to the conventional SCL cavities.

II. THEORY

The following dispersion relation pertaining to coupled-cavity linacs (CCLs) has been considered to take into account the phase advance of the EBG tank eigenmodes per cavity [22]:

$$k_1^2 \cos^2 \phi = \left(1 - \frac{f_a^2}{f_q^2} + k_a \cos 2\phi\right)\left(1 - \frac{f_c^2}{f_q^2} + k_c \cos 2\phi\right),$$
(1)

where f_a and f_c are the frequencies of the loaded accelerating cavities (ACs) and coupling cavities (CCs), respectively; k_a is the coupling constant between two consecutive ACs; k_c is the coupling constant between two consecutive CCs; k_1 is the coupling constant between ACs and CCs; $\phi = \pi q/2N$, $q = 0, 1, \ldots, 2N$ is the phase advance per cavity of the tank eigenmode with index q and frequency f_q; and N is the number of CCs and $N + 1$ is the number of ACs [22]. For $\phi = \pi/2$, the accelerating mode ($\pi/2$ mode) has two different frequencies: the frequency $f_{\pi/2}^{ac} = f_a/\sqrt{1 - k_a}$, depending on the chain of the coupled ACs, and the frequency $f_{\pi/2}^{cc} = f_c/\sqrt{1 - k_c}$, depending on the chain of the coupled CCs. The difference between $f_{\pi/2}^{ac}$ and $f_{\pi/2}^{cc}$ is the so-called stopband [22]. The geometry of ACs and CCs must be refined in order to minimize the stopband, that is, $f_{\pi/2}^{ac} \cong f_{\pi/2}^{cc}$.

The frequencies of ACs and CCs, f_a, f_c, and the coupling constants k_a, k_c, and k_1, in (1) can be calculated via the simulated linac eigenfrequencies f_q [21], [23]. For on-axis coupled linacs, according to the image theory [24], a five-cavity tank, or quintuplet, closed with half ACs has the same electromagnetic field distribution of an infinitely long tank (see Fig. 1). This allows us to calculate the five electromagnetic parameters f_a, f_c, k_1, k_a, and k_c by substituting in (1) the five

eigenfrequencies f_q, $q = 0, \ldots, 4$ of the simulated quintuplet closed with half ACs. Therefore, the following system of five polynomial equations is obtained:

$$\begin{cases} \left(1 - \frac{f_a^2}{f_0^2} + k_a\right)\left(1 - \frac{f_c^2}{f_0^2} + k_c\right) = k_1^2, & q = 0 \\ \left(1 - \frac{f_a^2}{f_1^2}\right)\left(1 - \frac{f_c^2}{f_1^2}\right) = \frac{k_1^2}{2}, & q = 1 \\ \left(1 - \frac{f_a^2}{f_2^2} - k_a\right)\left(1 - \frac{f_c^2}{f_2^2} - k_c\right) = 0, & q = 2 \\ \left(1 - \frac{f_a^2}{f_3^2}\right)\left(1 - \frac{f_c^2}{f_3^2}\right) = \frac{k_1^2}{2}, & q = 3 \\ \left(1 - \frac{f_a^2}{f_4^2} + k_a\right)\left(1 - \frac{f_c^2}{f_4^2} + k_c\right) = k_1^2, & q = 4. \end{cases}$$
(2)

The solution of the polynomial equation system in (2) is the array of the five unknowns $[f_a, f_c, k_1, k_a, k_c]^T$. The $\pi/2$ mode frequency is then calculated as $f_{\pi/2} = f_2 = f_a/\sqrt{1 - k_a}$.

A. End Cells

In actual linac plants, the tanks are closed with full ACs, referred to as end cells (ECs), to allow the beam to pass through. However, the theory described so far is also useful for the design of the ECs, since the resonant frequency of the ECs, f_e, depends on f_a and k_a. In fact, to preserve the electromagnetic field distribution of the $\pi/2$ mode of the linac tank, both the ECs are tuned so that their resonant frequency, f_e, is equal to [25]:

$$f_e = f_a \sqrt{\frac{1 - k_a/2}{1 - k_a}}$$
(3)

where f_a and k_a are obtained from the system in (2).

III. DESIGN

A sketch of the EBG ACs and CCs considered in the model are shown in Figs. 2 and 3, respectively. An octagonal lattice of cylindrical copper rods is considered, due to its eightfold
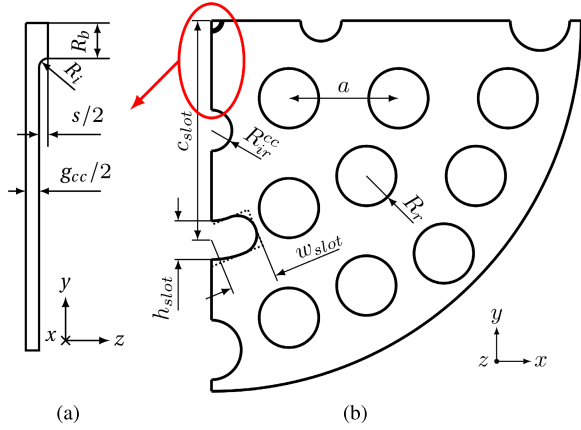
Fig. 3. Sketches of the (a) transversal and (b) longitudinal cross sections of an EBG CC. One-eighth of the total inner (vacuum) volume is shown. The rods overlapping with the coupling slot area are removed from the cavity. The geometrical parameters are listed in Tables I and III.

Fig. 5. Three-dimensional sketch of a full-EBG accelerating cavity. The outer (copper) volume is shown. The end wall with the 90°-rotated magnetic coupling slots is shown in transparency.
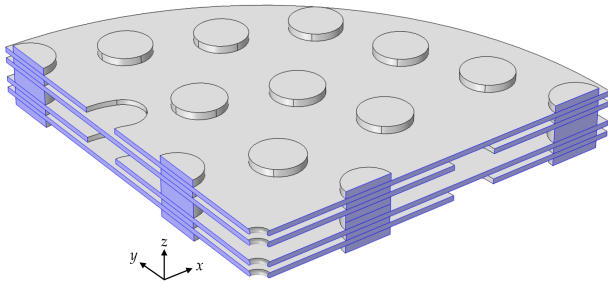

Fig. 4. Three-dimensional sketch of a quarter of an EBG quintuplet closed with half ACs. The outer (copper) volume is shown. The planes highlighted in blue are PMC planes. The xy-planes cutting the half ACs are PEC planes. The PMLs are not shown.

rotational symmetry, which, in turn, allows for twofold rotational symmetry when also considering the coupling slots. The confinement of the accelerating mode is obtained by removing one rod in the center of the 2-D metal lattice. The oxygen-free electronic grade copper is considered as the material for rods and plates [21].

To reduce the computational effort of simulations, the electromagnetic symmetry of the TM_{010}-like modes propagating in the ACs and CCs is exploited. In particular, as boundary conditions, the xz- and yz-planes are considered as perfect magnetic conducting (PMC) planes, while the xy-planes at half cavities are considered as perfect electric conducting (PEC) planes (see Fig. 4). Moreover, to take into account the open sides of ACs and CCs, the perfectly matched layers (PMLs) are used around the inner volumes of ACs and CCs. Three octagonal rings of rods are used in the design of ACs and CCs since the higher the number of rings, the higher the electromagnetic power losses.

Due to the open sides of the EBG cavities, the on-axis coupling between ACs and CCs is considered in the model. Two slots for magnetic coupling between ACs and CCs are placed on the end wall of each cavity. As an example, in Fig. 5, a 3-D sketch of an EBG accelerating cavity is shown. To avoid direct magnetic coupling between cavities of the same type, the coupling slots on one end wall are rotated by 90° from the coupling slots on the opposite end walls [22]. The rods
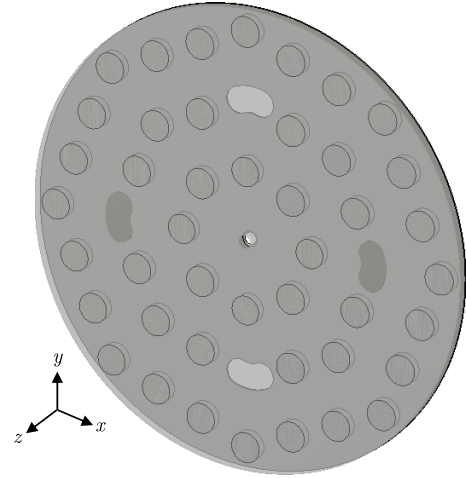
which overlap with the coupling apertures are removed from each cavity (see Figs. 2 and 3).

Since the electromagnetic field of the accelerating mode is confined in the center volume of the EBG cavities, the radius of the rods on the innermost ring strongly influences the resonance frequency of the cavities. The innermost rods placed below the coupling slots have a different radius ($R_{ir}^{ac,cc}$ in Figs. 2 and 3) from that of the other rods (R_r in Figs. 2 and 3). This is also done in order to achieve a finer tuning of the frequency of ACs and CCs, which is required for reducing the stopband or tuning the frequency of the end cells.

A. HA Code Details

The hybrid analytical/numerical approach used to design the linac EBG cavities is implemented via the HA code, whose block diagram is shown in Fig. 6. The HA code is effectively the same one described in [21] and successfully validated by measurements. To mitigate the computational effort and increase the efficiency, the HA code has been improved by means of a double-step optimization approach described in the following. The HA code integrates a 3-D numerical investigation based on a commercial FEM software with the analytical model described in Section II and an optimization routine. In particular, a multi-objective PSO technique [26]–[28] is used to find the optimal geometry of the linac EBG cavities by exploiting the Pareto optimality condition [29]. To this aim, the following components of the multi-objective function $O(x) = [o_1(x), o_2(x), o_3(x)]$ are simultaneously minimized:

$$o_1(x) = \left| f_{\pi/2}^{ac}(x) - f_{\pi/2,ref} \right|$$
$$o_2(x) = \left| f_{\pi/2}^{cc}(x) - f_{\pi/2,ref} \right|$$
$$o_3(x) = 1/ZT_{0,ac}^2(x) \qquad (4)$$

where x is the vector of the geometrical parameters to be optimized, listed in Table I, $f_{\pi/2,ref}$ is the reference value of the $\pi/2$ mode frequency, imposed by the design specifications (Section III-B), $ZT_{0,ac}^2$ is the unloaded effective
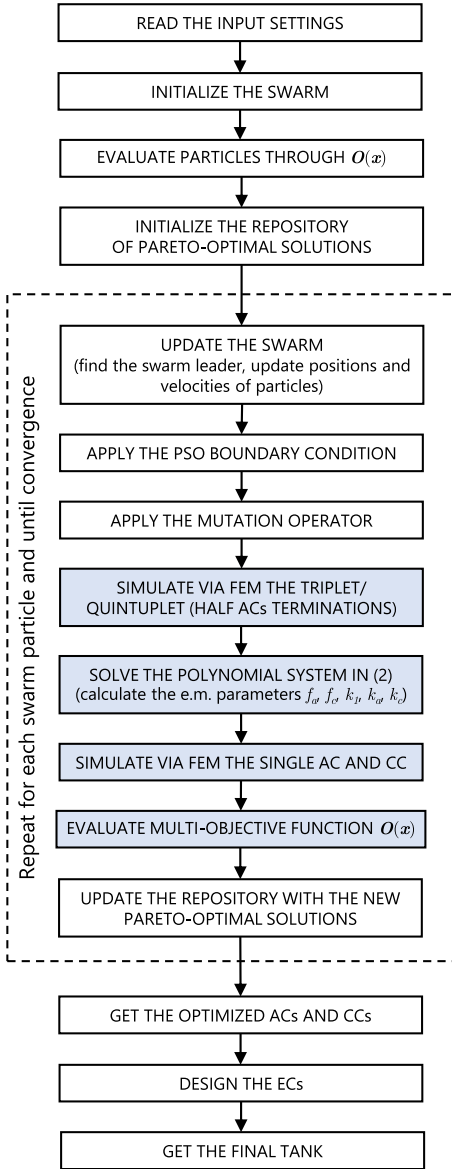
Fig. 6. Block diagram of the HA computer code used to design the EBG tank. The operations highlighted in blue are those involved in evaluating the position of a swarm particle.

shunt impedance per unit length of the ACs [22], and $f_{\pi/2}^{ac} = f_a/\sqrt{1-k_a}$ and $f_{\pi/2}^{cc} = f_c/\sqrt{1-k_c}$ are the two $\pi/2$ mode frequency solutions of (1); f_a, f_c, k_a, and k_c are the loaded (coupled) cavity frequencies and coupling constants calculated by solving the polynomial equation system in (2). It is worth noting that the simultaneous minimization of $o_1(x)$ and $o_2(x)$ allows the two $\pi/2$ mode frequencies, $f_{\pi/2}^{ac}(x)$ and $f_{\pi/2}^{cc}(x)$, to tend to $f_{\pi/2,\mathrm{ref}}$. As a consequence, the difference between $o_1(x)$ and $o_2(x)$, that is, the stopband, tends to zero. At the same time, the energy gain in a given accelerating gap for a given power loss is maximized, through $o_3(x)$. In Section IV-A, the uniformity of the accelerating electric field is taken into account. In particular, to have about the same energy gain in each AC, the relative standard deviation, σ_R, of the longitudinal electric field maxima is kept below a fixed threshold $\sigma_{R,\max}$. The details on the design constraints are given in Section III-B.

TABLE I
OPTIMIZED GEOMETRIES OF THE EBG ACs AND CCs

Parameter	Description	Search range (mm)	Optimized value (mm)
a	Lattice constant	[40.0, 50.0]	45.515
R_r	Radius of rods	[2.0, 20.0]	9.889
g_{ac}	ACs: gap length	[1.0, 6.0]	5.807
R_{ir}^{ac}	ACs: inner rods' radius	[2.0, 20.0]	9.483
R_{ir}^{cc}	CCs: inner rods' radius	[2.0, 20.0]	9.188
w_{slot}	Half-width of coupling slots	[12.0, 35.0]	17.219
h_{slot}	Height of coupling slots	[2.0, 35.0]	17.444

To evaluate the fitness of each swarm particle position, x, through the multi-objective function $O(x)$, the HA code drives the 3-D FEM numerical simulations of the linac EBG cavities. In particular, for each set of tentative geometrical parameters (tentative solution), x holds the following.

1) The eigenmodes of the single EBG cavities and the whole tank are simulated via FEM.
2) The analytical dispersion equation in (1) is calculated at each modal frequency of the tank.
3) The polynomial equation system in (2) is written and solved. The solution of the system gives the coupling constants and the loaded eigenfrequencies of the tentative ACs and CCs.
4) Then, the multi-objective function $O(x)$ in (4) is calculated.

To reduce the computational cost of numerical simulations, a double-step optimization approach has been used. The first optimization step is carried out by considering in the analytical model a three-cavity tank, or triplet, closed with half ACs. In this case, only the nearest-neighbor coupling is taken into account [22]. That is, the polynomial equation system in (2) reduces to three equations with the unknowns $[f_a, f_c, k_1]^T$ and $k_a = 0$, $k_c = 0$. Then, the second optimization step is carried out by considering quintuplets, that is, the complete system in (2) is taken into account. The second optimization step is a refinement of the first optimization step, and therefore, a very small number of iterations are needed in the second optimization step. By using this double-step approach, the design of the linac cavities needs less than half the time that would be required if only quintuplets were simulated at each HA code iteration, for equal mesh size and HA code settings. By using triplet simulations, the approximations $k_a = 0$ and $k_c = 0$ must be considered. However, if the coupling constants k_a and k_c are small, the accuracy of the optimization results is slightly affected by the above approximation (just a little tuning of the loaded cavity frequencies is needed in the second optimization step).

B. Design Specifications

The electromagnetic design of an on-axis coupled EBG proton linac tank consisting of 35 cavities (18 ACs and 17 CCs) is performed via the HA computer code. The average design velocity, $\beta = 0.24$, for the proton beam in the EBG tank has been calculated via an iterative procedure by taking into account the design parameters listed in Table II [30], [31].

TABLE II
HA CELL LENGTH COMPUTATION SETTINGS

Parameter	Description	Value
$f_{\pi/2,\text{ref}}$	Design $\pi/2$ mode frequency (GHz)	2.99792
β	Proton relative velocity	0.24
E_{in}	Proton beam input energy (MeV)	27
E_0	Average electric field on beam line (MV/m)	15
T	Nominal transit-time factor	0.80
ϕ_s	Synchronous phase (°)	-20
n_{ACs}	Total number of ACs in tank	18

TABLE III
CONSTANT GEOMETRICAL PARAMETERS OF THE EBG ACs AND CCs

Parameter	Description	Value (mm)
L	Accelerating tank period	12.14
R_b	Beam hole radius	4.00
R_i	Beam hole corner radius	1.00
s	Septum (wall) thickness	2.00
g_{cc}	CCs: gap length	$L - g_{ac} - 2s$
c_{slot}	Center of coupling slots	$2a$

The parameters listed in Table II are the same used for designing the conventional cavities of a 27-MeV 3-GHz proton SCL tank [21]. The accelerating tank period of the EBG tank is $L = \beta\lambda/2 = 12.140$ mm and it is listed in Table III. Moreover, the relative standard deviation of the longitudinal electric field peaks is kept below $\sigma_{R,\max} = 3\%$ in order to have a more uniform energy gain along the beamline. All the parameters described so far, in addition to the objectives in (4), represent the design specifications.

IV. SIMULATION RESULTS

Table I lists the optimized geometrical parameters of the EBG ACs and CCs, along with their search ranges. It is worth noting that the search ranges listed in Table I are wide enough to provide a large set of feasible solutions, that is, to provide swarm with very good exploratory capabilities and population diversity.

1) An initial guess of the lattice constant, a, is calculated by considering the central volume of the EBG cavities as it was a conventional TM_{010} cylindrical resonator. Then, a search range for the lattice constant is imposed around the initial guess.

2) In the second optimization step based on quintuplet simulations (see Section III-A), only the values of $R_{\text{ir}}^{\text{ac}}$ and $R_{\text{ir}}^{\text{cc}}$ are refined in the range [8.5, 9.5] mm, around the values optimized in the first step (9.376 and 9.233 mm, respectively), by keeping the other geometrical parameters at the values obtained by the first optimization.

Table III lists the parameters not involved in the optimization process, that is, no search ranges are defined for these parameters.

1) The beam hole radius, R_b, is set to a value, taken from the literature, providing high proton beam transmittance [21], [23], [32].

TABLE IV
HA OPTIMIZATION SETTINGS

Parameter	Description	Value
n_{iter}	Total number of iterations	$50 + 5^{\dagger}$
n_{pop}	Number of swarm particles	50
n_{rep}	Swarm particles repository size	100
w	Inertia weight	0.4
c_1	Cognitive constant	1
c_2	Social constant	1
n_{grid}	Adaptive grid divisions (in all dimensions)	30
M	Mutation rate	0.5

‡ Triplet + quintuplet optimizations.

2) The beam hole corner is rounded off by the radius R_i to reduce the field lines concentration, thus reducing thermal stress [21], [23], [32].

3) The gap length of CCs, g_{cc}, is always calculated such that the center-to-center axial distance between two consecutive ACs is equal to the tank period L (see Fig. 1).

The settings of the optimization routine are listed in Table IV. The values of w, c_1, c_2, n_{grid}, and M are the same suggested in [26]. The values of n_{iter}, n_{pop}, and n_{rep} are chosen in order to reduce the computational cost of the approach, while keeping a good population diversity and ensuring accurate results. Furthermore, the invisible boundary condition is imposed on the search space [33]. Several attempts were made to check the robustness of the HA code by using large search ranges and different population size and number of iterations, which are the most critical parameters for evolutionary optimization algorithms (due to fitness evaluations and overall computation time). The parameters listed in Table IV and the search space in Table I are a good tradeoff between computation time and convergence consistency. The uncertainties in the solutions of multiple runs range from 0.1% to 1%. Smaller uncertainties can be achieved by increasing n_{pop} and n_{iter} or by introducing a suitable convergence criterium taking into account at least the uncertainties of the most significant parameters.

The computation time needed to obtain the optimized geometrical parameters listed in Table I mainly depends on the mesh settings defined for 3-D FEM simulations. The maximum mesh size used in the HA code for 3-D FEM simulations is equal to $(c/f_{\pi/2,\text{ref}})/10$, where c is the speed of light in vacuum. By also considering the settings listed in Table IV, the electromagnetic symmetries described in Section III, and the double-step optimization approach described in Section III-A, the EBG tank design has required about two days on a PC with an Intel Core i7-4770 and 16 GB of RAM.

Table V lists the loaded frequencies and coupling constants of the optimized EBG cavities. The stopband is very small, being about 292 kHz.

A. End Cells

The results illustrated in Section IV are used for the design of the ECs. In particular, starting from the optimized ACs, the two ECs are then finely tuned so that: 1) the relative

TABLE V
FREQUENCIES AND COUPLING CONSTANTS OF
THE OPTIMIZED EBG CAVITIES

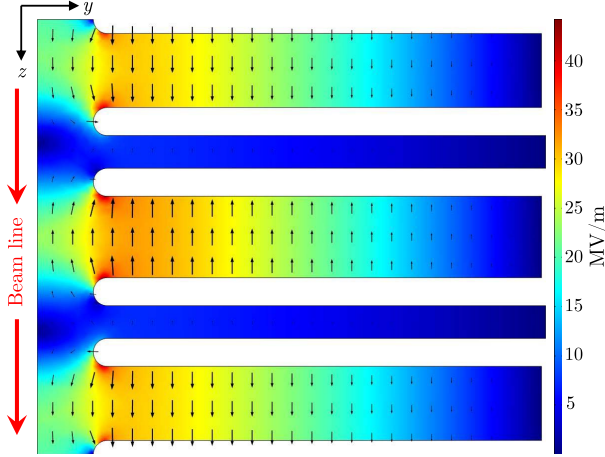| Parameter	Description	Value
f_a	Frequency of ACs (GHz)	2.998141
f_c	Frequency of CCs (GHz)	2.999258
k_1	Coupling constant between ACs and CCs	3.52×10^{-3}
k_a	Coupling constant between ACs	4.63×10^{-4}
k_c	Coupling constant between CCs	-8.69×10^{-5}

Fig. 7. Simulated electric field distribution of the $\pi/2$ mode in an EBG proton linac tank of five HA-optimized cavities closed with full ECs. The central volume of the EBG tank, enclosed by the innermost rods, is shown.

Fig. 8. Simulated longitudinal electric field intensity, $|E_z|$, along the beamline in an EBG proton linac tank of five HA-optimized cavities closed with full ECs.

TABLE VI
PERFORMANCE COMPARISON BETWEEN THE ACS OF AN SCL TANK
AND THE ACS OF THE PROPOSED EBG TANK

Parameter	SCL [21]	EBG
Unloaded frequency (GHz)	3.06231	2.99364
Cavity radius (mm)	33.563	151.434
Cavity length (mm)	12.140	7.807
Accelerating gap length (mm)	3.059	5.807
Average axial electric field (MV/m)	15	15
Transit-time factor	0.78	0.84
Unloaded quality factor	6180	4032
Surface losses (kW)	53.3	61.9
Effective shunt impedance per unit length (MΩ/m)	31	20
Peak surface electric field (MV/m)	93.2	32.6
Peak surface current density (kA/m)	37.8	51.1

standard deviation of the peaks of the longitudinal electric field intensity, $|E_z|$, is less than $\sigma_{R,\text{max}} = 3\%$ and 2) the $\pi/2$ mode frequency is equal (or very close) to $f_{\pi/2,\text{ref}}$. To this aim, the gap length of the ECs, g_{ec}, is slightly lowered with respect to the gap length of the optimized ACs, g_{ac}, that is, $g_{\text{ec}} = 0.91\,g_{\text{ac}}$. As an example, Fig. 7 shows the electric field distribution of the $\pi/2$ mode in a tank of five optimized EBG cavities closed with the ECs. The longitudinal electric field intensity, $|E_z|$, along the beamline of the same simulated tank is shown in Fig. 8, where the three peaks are obtained in the two ECs and in the center AC. In Figs. 7 and 8, the electric field intensity is normalized in order to have the mean value $E_0 = 15$ MV/m along the beamline (see Table II). Following the tuning of the ECs, the very small value $\sigma_R = 1.1\%$ is obtained and the simulated frequency of the $\pi/2$ mode is $f_{\pi/2,\text{sim}} = 2.99809$ GHz, which is very close to $f_{\pi/2,\text{ref}}$ (see Table II).

V. SCL ACS VERSUS EBG ACS

In Table VI, the performances of the optimized EBG accelerating cavities are compared with the performances of the accelerating cavities of a 27-MeV 3-GHz SCL tank [21]. The same design specifications on $f_{\pi/2,\text{ref}}$, E_{in}, E_0, and L (see Table II) are considered for both the EBG and SCL tanks.

The power losses of the EBG cavities are higher than those of the SCL cavities, due to the larger transversal dimension of the EBG cavities and to the on-axis coupling configuration.
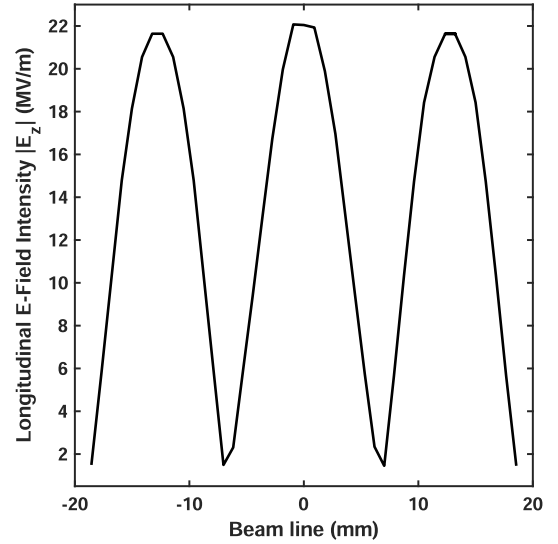
This, in turn, results in a 30% lower Q factor and effective shunt impedance. It is worth noting that, by considering higher $\pi/2$ mode frequencies and/or higher proton beam input energies, higher Q factor EBG cavities can be designed.

The transit time factor of the EBG cavities is about 8% higher than that of the SCL cavities, approaching values typically found in higher energy linac cavities [22], [31], [34]. Moreover, the peak surface electric field of the EBG cavities is strongly reduced, by about 65%. This is due to the absence of nose cones, which instead are needed in SCL cavities to increase the transit time factor. Since EBG and SCL accelerating cavities have the same $\beta\lambda$ and E_0 and the electric field is predominant near the beamline, the higher transit time factor of the EBG accelerating cavities may be related to the lower peak surface electric field, which results in lower thermal losses and better exploitation of the on-axis electric field to provide energy gain to the proton beam.
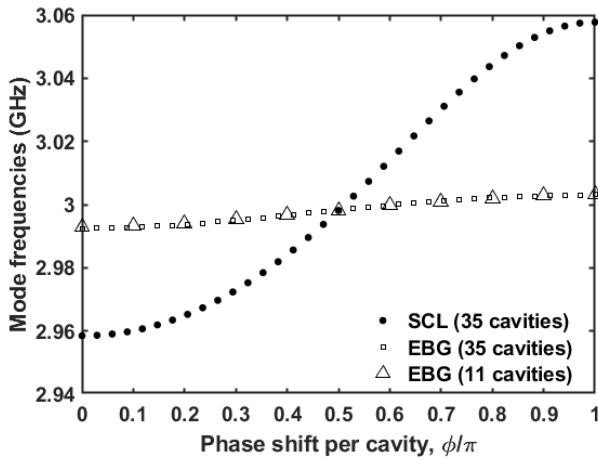
Fig. 9. Dispersion curves of the EBG tanks with 35 and 11 cavities (shown with square and triangle markers, respectively). The dispersion curve of the SCL tank with 35 cavities described in [21] is also shown.

The peak surface current density is about 35% higher in the EBG cavities due to the presence of the innermost rods which prevent the RF surface current from flowing over larger surfaces. The surface current density is higher at the rods' boundaries, where the magnetic field is predominant. To mitigate the peak surface current density on the rods' boundaries, two feasible solutions are: 1) add an objective component in (4) to minimize the peak magnetic flux and 2) placing suitable cooling pipes within the innermost rods. It is worth noting that such cooling pipes can also be effective for managing high thermal stress points near the beam hole corner, where the peak surface electric field is predominant.

In Fig. 9, the dispersion curve of the 35-cavities EBG tank is shown along with the dispersion curve of the 35-cavities SCL tank described in [21]. Because of the lower coupling constant k_1, the frequency spacing between the $\pi/2$ mode and the adjacent modes in the EBG tank is very small, being about 0.5 MHz, while in the SCL tank it is equal to about 4.4 MHz. However, from an RF point of view, by increasing the accelerating gradient in the EBG accelerating cavities by a factor of 3, one-third of the total number of ACs is enough to achieve the same energy gain. In Fig. 9, the dispersion curve of a shorter EBG tank with 11 cavities (4 ACs, 2 ECs, and 5 CCs) is also shown. In such a case, the frequency spacing between the $\pi/2$ mode and the adjacent modes increases to about 1.5 MHz. By increasing the accelerating gradient, the surface losses increase as well, making it necessary to consider higher $\pi/2$ mode frequencies. The maximization of the frequency difference between modes neighboring the $\pi/2$ mode can be included in the multi-objective function $O(x)$ in order to further increase the field distribution stability. A different geometry for the coupling slots and the innermost rods can also be investigated to increase the value of k_1.

In order to evaluate the wakefield damping provided by the EBG cavities, the longitudinal and transverse wake potentials and impedances have been numerically simulated with single-bunch excitation. The EBG quintuplet closed with the ECs has been considered and compared with the SCL counterpart described in [21]. A proton bunch with a gaussian line
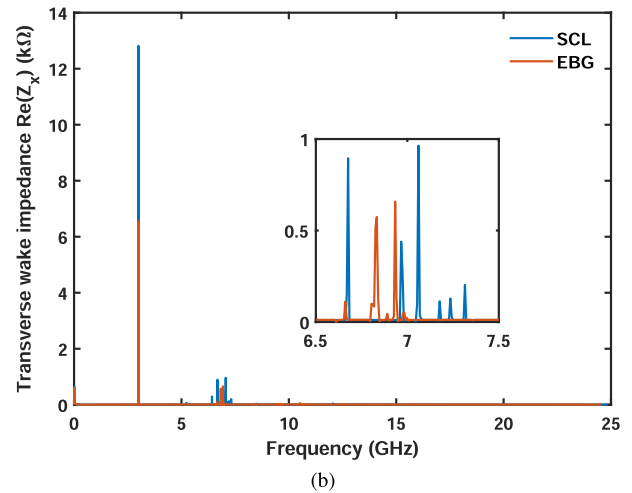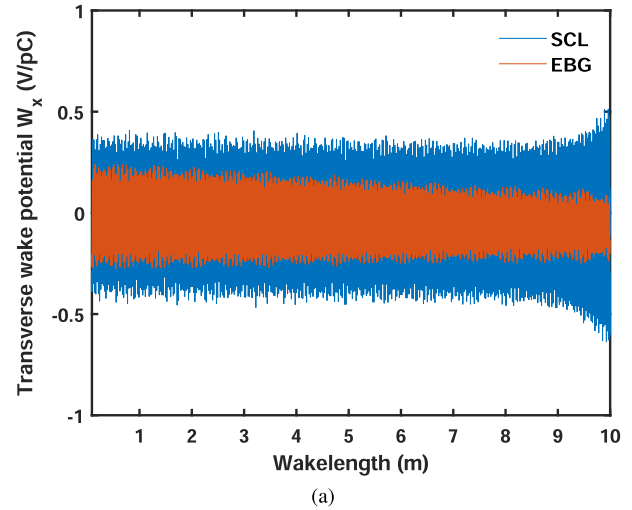

(a)

(b)

Fig. 10. (a) Numerical simulation of the transverse wake potential in the EBG structure on a line parallel to the beam propagation line and displaced 2 mm in the x-direction; the transverse wakes of the SCL structure in [21] is also shown for comparison. (b) Transverse wake impedances (spectra) of the EBG and SCL structures.

charge distribution, having a length of 1 mm and a relative velocity $\beta = 0.24$ (Table II), has been injected into the beam pipes of the linacs with a 2-mm displacement in the x-direction. The transverse wake potential is shown in Fig. 10 as a function of the wake length, that is, the distance behind the bunch. The transverse wake impedance, that is, the frequency spectrum of the wake fields, is also shown. The beam loading due to the fundamental TM_{010}-like monopole mode largely contribute to the transverse wakes of both tanks. The high Q factor of the TM_{010}-like mode involves a slow decay of the total transverse wake potential of the EBG tank. Conversely, in the SCL tank, the transverse wake potential remains at a stable value, even 10 m behind the exciting proton bunch (the small divergence in the tail may be due to the finite simulation length). The same also applies to the longitudinal wake potentials. The high-frequency components in the transverse wake spectra are due to the TM_{230}-like quadrupole mode, for the EBG tank, and to the TM_{120}-like dipole mode, for the SCL tank. To evaluate the contribution to the transverse wake potentials from each mode, the transverse wake impedances
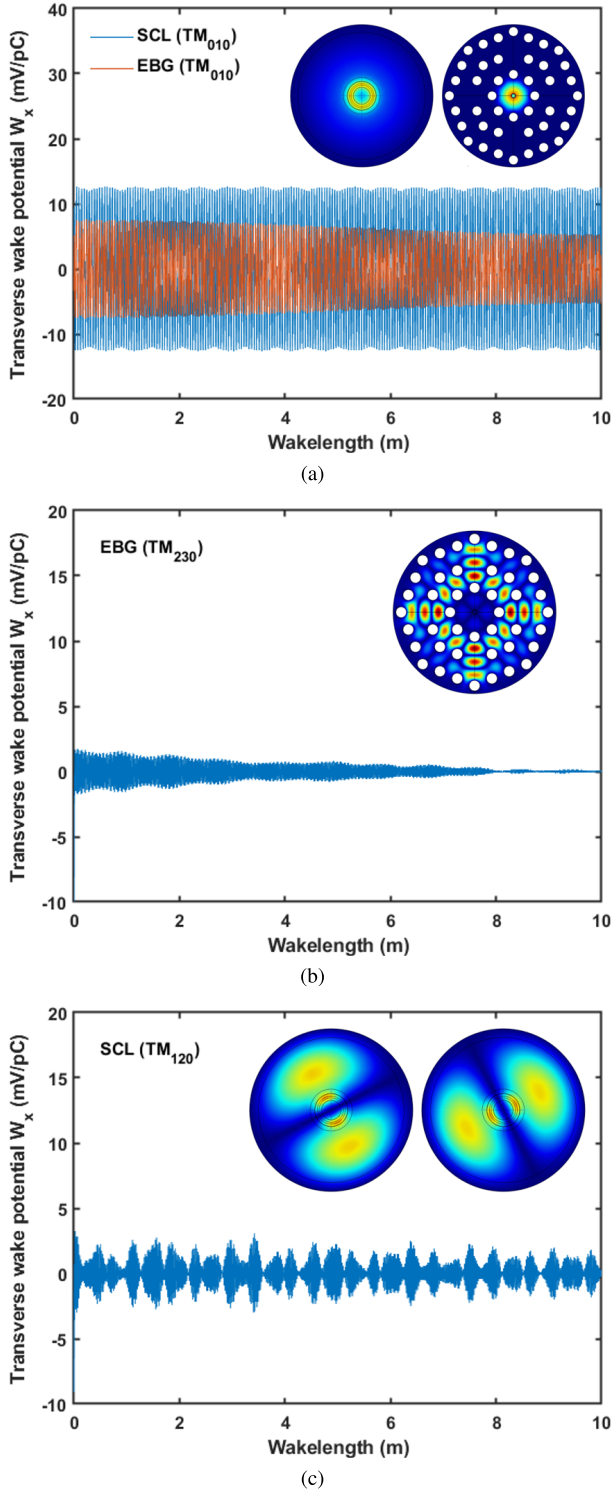
Fig. 11. Transverse wake potentials as a function of the wake length for each mode in the EBG and SCL structures. (a) TM_{010}-like fundamental modes (EBG and SCL). (b) TM_{230}-like quadrupole mode (EBG). (c) TM_{120}-like dipole mode (SCL).

have been filtered to isolate the peaks pertaining to each mode. Then, by means of an inverse fast Fourier transform, the wake damping due to each HOM has been recovered. Fig. 11 shows the separate contributions of the transverse wake potential as a function of the wake length. The transverse electromagnetic field distribution of the fundamental mode and HOMs are

also shown. As expected, the fundamental TM_{010}-like mode provides a slow-decaying transverse wake potential in the EBG tank and a constant transverse wake in the SCL tank. The TM_{230}-like quadrupole mode of the EBG tank is excited with less than half of the intensity of the fundamental mode. The faster decay of the TM_{230}-like mode is also due to the larger diffractive losses which lower its Q factor ($Q_{0,TM_{230}}^{EBG} = 1254$). Conversely, the higher Q factor of the TM_{120}-like dipole mode of the SCL ($Q_{0,TM_{120}}^{SCL} = 6852$) involves negligible damping of such HOM. These results confirm that the EBG cavities provide effective damping of the HOM wakefields relative to the SCL cavities.

Other advantages of EBG cavities with respect to SCL cavities are:
1) a smaller number of geometrical parameters, providing easier design;
2) an easier high-frequency scaling of the cavity transverse dimensions, which also allow higher accelerating gradients with negligible RF breakdown probability, according to the Kilpatrick criterion [22].

VI. CONCLUSION

A novel proton linac based on on-axis coupled EBG cavities has been designed. The design of the EBG cavities has been performed via the HA code, implementing a hybrid numerical/analytical approach [21]. The hybrid strategy has been used to design a 27-MeV 3-GHz EBG tank closed with full end cells. The simulated frequency of the EBG tank $\pi/2$ mode is $f_{\pi/2,\text{sim}} = 2.99809$ GHz, which is very close to the nominal value $f_{\pi/2,\text{ref}} = 2.99792$ GHz. The calculated stopband is very small, being about 292 kHz. Moreover, an accelerating field nonuniformity as small as $\sigma_R = 1.1\%$ has been calculated. The typical linac figures of merit of the optimized EBG accelerating cavities have been compared with those pertaining to the accelerating cavities of a 27-MeV 3-GHz SCL tank having the same accelerating period $L = 12.14$ mm, proton beta $\beta = 0.24$, and accelerating field gradient $E_0 = 15$ MV/m. The transit time factor of the EBG accelerating cavities is about 8% higher (SCL: 0.78 and EBG: 0.84), approaching values typically found in higher energy linac cavities. The Q factor of the EBG accelerating cavities is about 30% lower (SCL: 6180, EBG: 4032), suggesting considering higher $\pi/2$ mode frequency and/or higher proton beam input energy. Furthermore, the peak surface electric field in the EBG accelerating cavities is about 65% lower (SCL: 93.2 MV/m and EBG: 32.6 MV/m). Thus, EBG cavities are very promising for the design of higher frequency and higher accelerating gradient proton linacs with low RF breakdown probability. As an example, by considering the Kilpatrick limit $E_k = 46.8$ MV/m at $f_{\pi/2,\text{ref}}$, a conservative peak surface electric field $E_s = 2E_k$ would allow increasing the accelerating gradient of the EBG tank by about three times ($E_0 = 45$ MV/m), thus reducing to one-third its length. Higher values of $f_{\pi/2,\text{ref}}$ would enable even higher accelerating gradients and more compact tanks and lower losses. The longitudinal and transverse wake potentials excited by the proton beam in the EBG and SCL structures have been simulated and compared too. The contribution to the transverse wake potentials from

each HOM has been recovered. The results confirm that the EBG structure effectively damps the transverse wake potential due to HOMs. As the value of $f_{\pi/2,\mathrm{ref}}$ increases, other design constraints, such as the fabrication tolerances, the thermal stress at the innermost rod joints, and the increasing wakefield effects, must be carefully considered.

REFERENCES

[1] Y. Kasahara, H. Toyao, and E. Hankui, "Compact and multiband electromagnetic bandgap structures with adjustable bandgaps derived from branched open-circuit lines," *IEEE Trans. Microw. Theory Techn.*, vol. 65, no. 7, pp. 2330–2340, Jul. 2017.

[2] P.-S. Wei, M.-H. Tsai, S.-K. Hsu, C.-K. Shen, and T.-L. Wu, "An electromagnetic bandgap structure integrated with RF LNA using integrated fan-out wafer-level package for gigahertz noise suppression," *IEEE Trans. Microw. Theory Techn.*, vol. 66, no. 12, pp. 5482–5490, Dec. 2018.

[3] I. Ederra *et al.*, "Electromagnetic-bandgap waveguide for the millimeter range," *IEEE Trans. Microw. Theory Techn.*, vol. 58, no. 7, pp. 1734–1741, Jul. 2010.

[4] H. U. Habiba, K. Malathi, M. H. Masood, and R. Kunnath, "Tunable electromagnetic band gap-embedded multimode resonators for ultra-wideband dual band, lower-ultra-wideband and upper-ultra-wideband applications," *IET Microw., Antennas Propag.*, vol. 5, no. 10, pp. 1182–1187, 2011.

[5] J. de Dios Ruiz, F. L. Martinez-Viviente, A. Alvarez-Melcon, and J. Hinojosa, "Substrate integrated waveguide (SIW) with koch fractal electromagnetic bandgap structures (KFEBG) for bandpass filter design," *IEEE Microw. Wireless Compon. Lett.*, vol. 25, no. 3, pp. 160–162, Mar. 2015.

[6] Y. Guo, S. Kim, H. Gao, and G.-P. Li, "Compact high q configurable quint-band electromagnetic bandgap filter," *IEEE Access*, vol. 6, pp. 63703–63711, 2018.

[7] B. A. Zeb, Y. Ge, K. P. Esselle, Z. Sun, and M. E. Tobar, "A simple dual-band electromagnetic band gap resonator antenna based on inverted reflection phase gradient," *IEEE Trans. Antennas Propag.*, vol. 60, no. 10, pp. 4522–4529, Oct. 2012.

[8] W. Chen, C. A. Balanis, and C. R. Birtcher, "Checkerboard EBG surfaces for wideband radar cross section reduction," *IEEE Trans. Antennas Propag.*, vol. 63, no. 6, pp. 2636–2645, Jun. 2015.

[9] C. Huang, C. Ji, X. Wu, J. Song, and X. Luo, "Combining FSS and EBG surfaces for high-efficiency transmission and low-scattering properties," *IEEE Trans. Antennas Propag.*, vol. 66, no. 3, pp. 1628–1632, Mar. 2018.

[10] S. Y. Jun, B. Sanz Izquierdo, and E. A. Parker, "Liquid Sensor/Detector using an EBG structure," *IEEE Trans. Antennas Propag.*, vol. 67, no. 5, pp. 3366–3373, May 2019.

[11] M. A. Shapiro, W. J. Brown, I. Mastovsky, J. R. Sirigiri, and R. J. Temkin, "17 GHz photonic band gap cavity with improved input coupling," *Phys. Rev. Special Topics-Accel. Beams*, vol. 4, no. 4, Apr. 2001, Art. no. 042001.

[12] E. I. Smirnova, A. S. Kesar, I. Mastovsky, M. A. Shapiro, and R. J. Temkin, "Demonstration of a 17-GHz, high-gradient accelerator with a Photonic-Band-Gap structure," *Phys. Rev. Lett.*, vol. 95, no. 7, Aug. 2005, Art. no. 074801.

[13] E. I. Smirnova, I. Mastovsky, M. A. Shapiro, R. J. Temkin, L. M. Earley, and R. L. Edwards, "Fabrication and cold test of photonic band gap resonators and accelerator structures," *Phys. Rev. Special Topics-Accel. Beams*, vol. 8, no. 9, Sep. 2005, Art. no. 091302.

[14] B. J. Munroe, J. Zhang, H. Xu, M. A. Shapiro, and R. J. Temkin, "Experimental high gradient testing of a 17.1 GHz photonic band-gap accelerator structure," *Phys. Rev. Accel. Beams*, vol. 19, no. 3, Mar. 2016, Art. no. 031301.

[15] M. R. Masullo *et al.*, "Study of hybrid photonic band gap resonators for particle accelerators," *Microw. Opt. Technol. Lett.*, vol. 48, no. 12, pp. 2486–2491, Dec. 2006.

[16] E. Di Gennaro *et al.*, "Mode confinement in photonic quasicrystal point-defect cavities for particle accelerators," *Appl. Phys. Lett.*, vol. 93, no. 16, Oct. 2008, Art. no. 164102.

[17] E. Di Gennaro *et al.*, "Hybrid photonic-bandgap accelerating cavities," *New J. Phys.*, vol. 11, no. 11, 2009, Art. no. 113022.

[18] J. Zhang, B. J. Munroe, H. Xu, M. A. Shapiro, and R. J. Temkin, "High power experimental studies of hybrid photonic band gap accelerator structures," *Phys. Rev. Accel. Beams*, vol. 19, no. 8, Aug. 2016, Art. no. 081304.

[19] M. Hu, B. J. Munroe, M. A. Shapiro, and R. J. Temkin, "Calculation of wakefields in a 17 GHz beam-driven photonic band-gap accelerator structure," *Phys. Rev. Special Topics-Accel. Beams*, vol. 16, no. 2, Feb. 2013, Art. no. 022002.

[20] C. A. Bauer, G. R. Werner, and J. R. Cary, "Origin and reduction of wakefields in photonic crystal accelerator cavities," *Phys. Rev. Special Topics-Accel. Beams*, vol. 17, no. 5, May 2014, Art. no. 051301.

[21] D. Laneve *et al.*, "Electromagnetic design of microwave cavities for side-coupled linear accelerators: A hybrid Numerical/Analytical approach," *IEEE Trans. Nucl. Sci.*, vol. 65, no. 8, pp. 2233–2239, Aug. 2018.

[22] T. P. Wangler, *RF Linear Accelerators*, 2nd ed. Weinheim, Germany: Wiley, 2008.

[23] U. Amaldi, S. Braccini, and P. Puggioni, "High frequency linacs for hadrontherapy," *Rev. Accel. Sci. Technol.*, vol. 2, no. 1, pp. 111–131, 2009.

[24] C. A. Balanis, *Advanced Engineering Electromagnetics*, 2nd ed. Hoboken, NJ, USA: Wiley, 2012.

[25] O. Shanker, "Generalization of linac mode spectrum and fitting procedure," *Rev. Sci. Instrum.*, vol. 63, no. 10, pp. 4443–4445, Oct. 1992.

[26] C. A. C. Coello, G. T. Pulido, and M. S. Lechuga, "Handling multiple objectives with particle swarm optimization," *IEEE Trans. Evol. Comput.*, vol. 8, no. 3, pp. 256–279, Jun. 2004.

[27] M. C. Falconi *et al.*, "Dysprosium-doped chalcogenide master oscillator power amplifier (MOPA) for mid-IR emission," *J. Lightw. Technol.*, vol. 35, no. 2, pp. 265–273, Jan. 15, 2017.

[28] G. Palma *et al.*, "Novel double step approach for optical sensing via microsphere WGM resonance," *Opt. Express*, vol. 24, no. 23, pp. 26956–26971, Nov. 2016.

[29] C. A. Coello Coello, G. B. Lamont, and D. A. van Veldhuizen, *Evolutionary Algorithms for Solving Multi-Objective Problems*, 2nd ed. New York, NY, USA: Springer, 2007.

[30] K. Crandall, "Documentation for program design," Tech. Rep., 2006.

[31] L. Picardi, C. Ronsivalle, and A. Vignati, "Progetto del top linac," ENEA Res. Centre, Frascati, Italy, Tech. Rep. RT/INN/97/17, Jul. 1997.

[32] U. Amaldi *et al.*, "Accelerators for hadrontherapy: From lawrence cyclotrons to linacs," *Nucl. Instrum. Methods Phys. Res. A, Accel., Spectrometers, Detectors Associated Equip.*, vol. 620, nos. 2–3, pp. 563–577, Aug. 2010.

[33] J. Robinson and Y. Rahmat-Samii, "Particle swarm optimization in electromagnetics," *IEEE Trans. Antennas Propag.*, vol. 52, no. 2, pp. 397–407, Feb. 2004.

[34] C. Ronsivalle *et al.*, "The TOP-IMPLART project," *Eur. Phys. J. Plus*, vol. 126, no. 7, pp. 1–15, Jul. 2011.

[35] E. I. Simakov *et al.*, "Observation of wakefield suppression in a photonic-band-gap accelerator structure," *Phys. Rev. Lett.*, vol. 116, no. 6, Feb. 2016, Art. no. 064801.